Femtosecond 8.5 μm source based on intrapulse difference-frequency generation of 2.1 μm pulses

Ondřej Novák[1], Peter R. Krogen[2,3,4], Tobias Kroh[2,3,4], Tomáš Mocek[1], Franz X. Kärtner[2,3,4], and Kyung-Han Hong[2,*]

[1]*HiLASE Centre, Institute of Physics of the Czech Academy of Sciences, Za Radnicí 828, 252 41 Dolní Břežany, Czech Republic*
[2]*Research Laboratory of Electronics, Massachusetts Institute of Technology (MIT), Cambridge, Massachusetts 02139, USA*
[3]*Center for Free-Electron Laser Science and Deutsches Elektronen-Synchrotron (DESY), Notkestraße 85, 22607 Hamburg, Germany*
[4]*Department of Physics and Center for Ultrafast Imaging, University of Hamburg, Luruper Chaussee 149, 22761 Hamburg, Germany*
**Corresponding author: kyunghan@mit.edu*

Received XX Month XXXX; revised XX Month, XXXX; accepted XX Month XXXX; posted XX Month XXXX (Doc. ID XXXXX); published XX Month XXXX

We report on a femtosecond ~8.5 μm, ~2 μJ source based on the intrapulse difference-frequency generation (DFG) of 2.1 μm pulses in an $AgGaSe_2$ (AGSe) crystal. Compared to the conventional ~0.8 or 1 μm near-infrared (IR) pulses, a ~2 μm driver for intrapulse DFG can provide more efficient conversion into the wavelengths longer than 5 μm due to a lower quantum defect and is more suitable for the non-oxide nonlinear crystals that have a relatively low bandgap energy. Using 26 fs, 2.1 μm pulses for type-II intrapulse DFG we have generated intrinsically carrier-envelope phase-stable idler pulses with a conversion efficiency of 0.8%, which covers the wavelength range of 7–11 μm. Our simulation study shows that the blueshift of intrapulse DFG is assisted by self-phase modulation of the driving pulses in AGSe. The idler pulses are particularly useful for strong-field experiments in nanostructures as well as for seeding parametric amplifiers in the long-wavelength IR.

OCIS codes: *(140.3070) Infrared and far-infrared lasers; (190.4360) Nonlinear optics, devices; (190.4410) Nonlinear optics, parametric processes; (190.7110) Ultrafast nonlinear optics.*

Few-cycle carrier-envelope phase (CEP) stable mid-infrared (mid-IR) laser pulses are extremely useful for the scaling and precise control of strong-field electron dynamics in various media. Mid-IR-driven high-harmonic generation (HHG) in gases enables to extend the coherent soft X-ray photon energies to the water-window and keV range [1, 2] via cutoff energy scaling. Recently, sub-cycle electron dynamics in condensed matter have extensively been studied via HHG in bulk solids driven by mid-IR laser pulses [3, 4]. Sub-cycle tunneling in nano-structures [5, 6] can benefit from mid-IR drivers as well due to the stronger dependence on CEP than with near-IR drivers. In particular, long-wavelength IR (8–15 μm) few-cycle laser sources are of great interest for these applications.

The intrapulse DFG of broadband pulses has been widely used for producing CEP-stable pulses due to its passive stabilization mechanism. The subtraction of the equal phases of the shorter (pump) and longer (signal) wavelength spectral components of the broadband driving pulses leads to a constant phase of the idler pulse [7, 8]. So far intrapulse DFG has been demonstrated only with near-IR driver pulses. For example, CEP-stable pulses at ~2 μm were obtained by intrapulse DFG of 0.8 μm Ti:sapphire laser pulses in a periodically-poled lithium niobate crystal for seeding a ~2 μm optical parametric chirped-pulse amplifier (OPCPA) [9, 10]. The intrapulse DFG of Ti:sapphire laser pulses also resulted in the spectral coverage of 3–7 μm centered at 5 μm in $LiIO_3$ crystal [11], 2–4 μm in BiB_2O_6, or 2–5 μm in $KTiOAsO_4$ [12]. Pupeza *et al.* demonstrated intrapulse DFG in a $LiGaS_2$ crystal of externally compressed, 1 μm Yb:YAG laser pulses to cover the spectral region from 6.8 to 16.4 μm (at –30 dB) [13]. Intrapulse DFG based on supercontinuum generation from an Er:fiber system was used for the CEP stabilization of 1.55 μm pulses [14].

However, the efficiency and output pulse energy from intrapulse DFG are rather low and therefore the usage of a mid-IR driver can help to extend the idler wavelength into the long-wave IR with a better efficiency. Compared to the conventional ~0.8 or 1 μm near-IR pulses for intrapulse DFG, a ~2 μm driver can clearly provide much more efficient conversion due to a two times lower quantum defect. Moreover, ~2 μm is more suitable for pumping the non-oxide nonlinear crystals that have a relatively low bandgap energy without inducing linear or two-photon absorption. For these reasons, the 2-μm-pumped OPCPA and optical parametric amplifier (OPA) in either $ZnGeP_2$ or $CdSiP_2$ crystal have been demonstrated to reach the idler wavelengths up to ~5-10 μm [4, 15, 16]. More importantly, advanced ultrafast lasers at ~2-3 μm [15-18] promise simplification of the setup and increase in conversion efficiency of mid-IR OPCPA/OPA's.

In this Letter we demonstrate femtosecond intrapulse DFG in an $AgGaSe_2$ (AGSe) crystal driven by few-cycle 2.1 μm pulses. The idler pulses of 8.5 μm central wavelength and 2 μJ pulse energy are generated with 0.8% conversion efficiency. Intrinsic CEP stability is ensured by the intrapulse DFG process. We believe this is the first demonstration of intrapulse DFG with a ~2 μm beam. The basic setup, which comprises a half-wave plate, lens, and an AGSe crystal, is very simple and can be easily incorporated into any available femtosecond ~2 μm laser sources. The intrapulse DFG driven by a single broadband pulse is naturally synchronized and, unlike the conventional DFG, does not need any pulse delay adjustment.

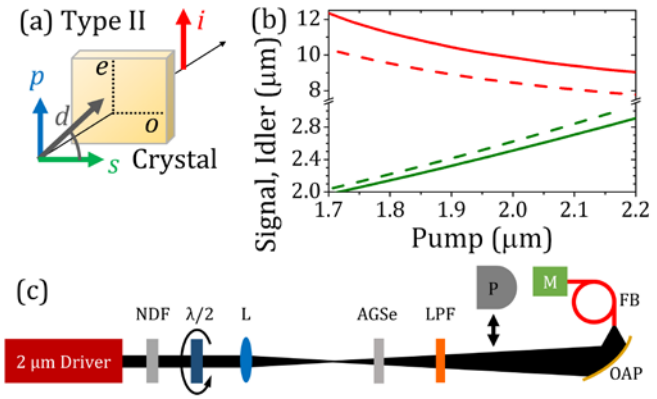

Fig. 1 (Color online) Type II DFG phase-matching scheme (a) in negative uniaxial birefringent crystals. Arrows indicate polarization (*d*, driver; *p*, pump; *s*, signal; *i*, idler) or axis (o, ordinary axis; *e*, extraordinary axis). (b) Signal (green) and idler (red) phase-matching curves of type II for $\theta = 53.1°$ (solid) and $\theta = 56.5°$ (dashed). (c) Schematic of the experimental setup for intrapulse DFG. NDF, neutral density filter; λ/2, half-wave plate at 2020 nm in a rotation mount; L, lens; AGSe, 2-mm-thick AGSe crystal; LPF, long pass filter; P, power meter; OAP, off-axis parabola; FB, mid-IR fiber; M, mid-IR monochromator with MCT detector.

The ~2 μm drive wavelength is within the transparency range of most non-oxide nonlinear optical crystals, which are transparent well beyond 5 μm. We have selected an AGSe crystal due to its favorable phase matching (PM) of DFG and broad transparency range of 0.8–18 μm, which is one of the broadest among the non-oxide crystals. Driving at ~2 μm dramatically reduces two-photon absorption as well. Extraordinary pump wave and ordinary signal wave are common for both type-I and -II PM schemes. The linearly-polarized driving beam is split into the ordinary and extraordinary polarization in the intrapulse DFG. The idler wave is on the ordinary and extraordinary axis in type I and type II, respectively. The type-II PM is preferred because of a higher effective second-order nonlinear coefficient, d_{eff}, with AGSe. Fig. 1(a) depicts the input polarization state in the type-II PM while Fig. 1(b) shows type-II PM curves for PM angle $\theta = 53.1°$ and $\theta = 56.5°$. The larger is the PM angle the longer (shorter) is the phase-matched signal (idler) wavelength for a given pump wavelength. A 2-mm-thick AGSe crystal used in the experiment is cut at $\theta = 53.1°$ and $\varphi = 0°$ for the normal incidence of the laser beam. Such PM enables e.g. following interaction $1/(1.88\,\mu m) - 1/(2.28\,\mu m) \rightarrow 1/(10.6\,\mu m)$, for which the type-II $d_{eff} = 33.9$ pm/V. Note that at $\varphi = 0°$, d_{eff} is zero for type-I PM, whereas $\theta = 45.7°$ and $\varphi = 45°$ are optimal for type-I PM. However, type-I $d_{eff} = 25.8$ pm/V is still smaller than the type-II PM case.

The driving pulses for intrapulse DFG stem from a CEP-stable 2.1 μm OPCPA generating multi-mJ, 26 fs pulses at a 1 kHz repetition rate [4, 10]. The output spectrum spans from 1.85 μm to 2.3 μm at 10% of maximum. The schematic of our experimental setup for the intrapulse DFG is straightforward and shown in Fig. 1(c). The 2.1 μm beam is attenuated using a variable neutral-density filter to a pulse energy of 250 μJ. The beam polarization is changed using a zero-order half-wave plate (half wave retardation at 2020 nm, WPH10M-2020, Thorlabs) to split the beam between *o*-wave and *e*-wave in the crystal, which is needed for type-II intrapulse DFG. Then the beam is focused by a 1025 mm focal length CaF_2 lens. The AGSe crystal is placed about 300 mm behind the focus in order to avoid the damage on the crystal. The estimated peak intensity is ~200 GW/cm². The 2.1 μm beam is filtered out by one of two long-pass filters (LPF's) with a cut-on wavelength of 4.5 μm or 2.4 μm behind the AGSe crystal on the way to the diagnostics part of the setup. The idler power and spectrum are measured behind the LPF. The off-axis parabola couples the beam into a multimode mid-IR fiber with a transmission range from 3 to 15 μm. The fiber is connected to a scanning-type grating monochromator (Horiba) with a liquid nitrogen cooled HgCdTe (MCT) detector.

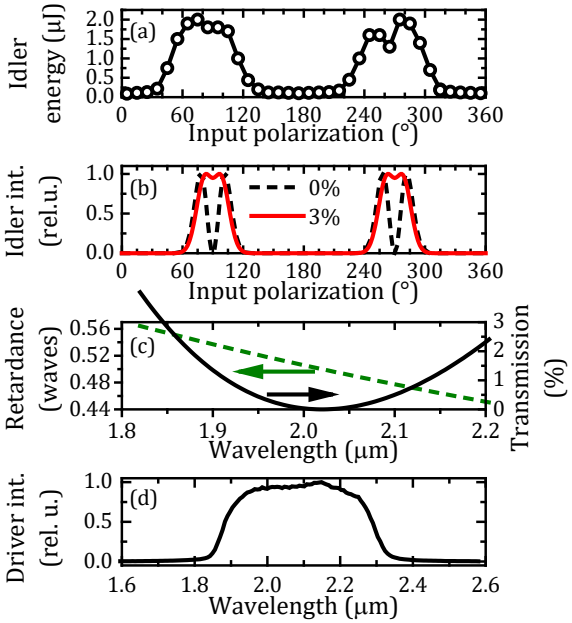

Fig. 2 Dependence of idler pulse energy (or intensity) on the input polarization angle (a) measured and (b) calculated – see text for explanation. (c) Retardance (dashed) and transmission (solid) for the used half-wave plate. Transmission means case when the wave plate rotates the polarization by 90° at its central wavelength and it is placed between parallel polarizers. (d) Optical spectrum of the driving pulse.

We first optimize the ratio between the extraordinary (pump part; angle 90° or 270°) and ordinary (signal part; angle 0° or 180°) waves in the crystal using the half-wave plate while monitoring the output energy of the DFG idler pulses. The dependence of idler energy measured after the 4.5 μm LPF on the input polarization angle of the driver beam is shown in Fig. 2(a). A maximum idler pulse energy of ~2 μJ is measured for a beam polarization of ~80° and ~280° relative to the ordinary axis of AGSe, where most of the drive beam corresponds to the extraordinary axis. The peaks are

relatively broad with a full-width at half-maximum (FWHM) bandwidth of ~65° in the two regions centered at 90° and 270°, respectively. This result indicates that the majority of the driver energy is used for the pump part (extraordinary axis), resembling the case of OPA with strong pump and weak signal. Conversion efficiency of ~0.8 % with respect to the total energy of the 2.1 μm beam (250 μJ) incident onto AGSe crystal is achieved experimentally. When the pulse energy is only in the ordinary wave (near 180° and 360° in Fig. 2(a)) the measured output energy is only 0.1 μJ, but it does not drop to zero as was expected. This can be attributed to the imperfect half-wave retardation outside the wavelength of 2020 nm, as shown in Figs. 2(c) and (d). There is a weak idler generated even if the average beam polarization is along in ordinary wave due to the leakage into the extraordinary axis. The polarization leakage becomes even more significant with the spectral broadening of the driver pulse in AGSe owing to self-phase modulation (SPM), as discussed later.

Simple calculations help to understand the observed dependence on the input polarization. In the undepleted regime the idler output intensity is determined by the product of gain and input signal intensity. The gain is proportional to pump intensity as $\sinh^2\left(\gamma L\sqrt{I_p}\right)$, where γ is the gain coefficient, L is the crystal length and I_p is the pump intensity. Theoretically, if either the signal or pump beam intensity is zero, the resulting idler intensity is zero as well. In other words, when the polarization of the driver beam is perfectly in the principal plane (0/180°) or perpendicular to it (90/270°), the idler output ideally becomes zero (Fig. 2(b), dashed line). In this case the idler intensity dependence has four peaks with the tuning of 0–360°. As indicated by all the four peaks closer to 90/270° than 0/180°, the pump intensity is higher than the signal intensity for high conversion efficiency.

In our experiment the polarization of the few-cycle driver pulse is not perfectly the same over the entire driver bandwidth because the retardance still slightly varies with wavelength even with the zero-order waveplate (see Fig. 2(c), dashed line). As a result both polarization components always coexist. For example, if we assume a constant leakage of ~3% into the other polarization components independent of the waveplate setting, the calculated dependence changes significantly. The dips in the idler output dependence on input beam polarization at angles of 90° and 270° almost disappear (Fig. 2(b), solid line). The four-peak structure reduces to a two-peak structure, as observed experimentally in Fig. 2(a). Therefore, the small leakage of polarization qualitatively explains the experimental observation very well.

The idler spectrum, shown in Fig. 3(a), is measured for the pump polarization outputting the highest idler energy. It shows a peak at ~8.5 μm and has a bandwidth of 1.4 μm in FWHM. Note that the total bandwidth covers ~6.2 μm in full width at 1% maximum, *i.e.*, more than an octave, as indicated by the inset of Fig. 3(a). The intrapulse DFG process is further investigated using (2+1)-dimensional numerical simulations [19]. A Gaussian temporal profile with 26 fs duration (FWHM) and spatial profile with 3.4 mm $1/e^2$ diameter is used for simulations. We also include SPM and self-focusing into the calculations as well because of the high nonlinear refractive index of AGSe, $n_2 = 350 \times 10^{-16}$ cm^2/W [20]. The PM angle was set to θ = 56.5°. The calculated spectrum (Fig. 3(b)) shows a quantitative agreement with the measured one (Fig. 3(a)). The peak is at 8.8 μm and the bandwidth is 1.47 μm (FWHM). The calculated pulse duration (inset of Fig. 3(b)) of the idler pulse is 80 fs (FWHM), corresponding to sub-3 optical cycles.

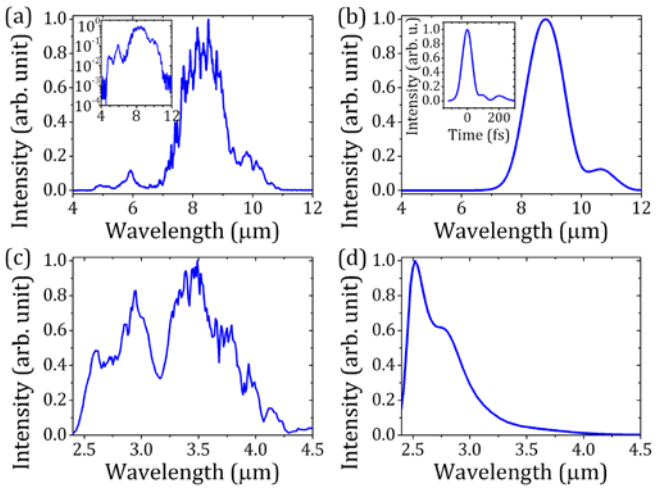

Fig. 3 Spectrum of the generated idler (a) measured behind the 4.5 μm band-pass filter (inset shows the same spectrum in log scale) and (b) calculated spectrum. Inset of (b) shows calculated uncompressed idler temporal pulse profile. Spectrum beyond 2.4 μm (c) measured and (d) calculated corresponding to ordinary field, i.e. signal part of the output driving pulse. Calculated spectrum includes fiber and filter response.

While the design wavelength for intrapulse DFG was originally targeted at ~10 μm, the dominant spectral component of the idler pulse is found to be blueshifted to 8.5 μm. According to the PM curve for θ=56.5° this wavelength can be generated by the pump and signal wavelengths of ~2.0 and ~2.6 μm, respectively. However, since the spectral content at ~2.6 μm is quite low (~–30 dB) in the incident beam, an obvious question needs to be answered: why does the idler peak correspond to this wavelength of signal? The blueshift of the idler wavelength can be explained by the spectral broadening and amplification of the incident pulse to beyond 2.6 μm. Our simulation has confirmed that SPM plays an important role here. The spectral broadening is clearly shown by the measured output spectrum with the 2.4 μm LPF, shown as Fig. 3(c). The experimental spectrum spans up to ~4.3 μm, whereas the calculated one reaches only up to ~3.5 μm (Fig. 3(d)). It should be noted that the 2.4 μm LPF and the mid-IR fiber are responsible for the low transmission below ~2.6 μm. Calculations may not catch all the nonlinear interactions that occur in the experiment, but the SPM-induced spectral broadening beyond 2.6 μm satisfactorily explains the blueshift of the idler spectrum from ~10 to ~8.5 μm with presumably higher efficiency.

The intrapulse DFG results in intrinsically CEP-stable idler pulses. However, the CEP stability could be degraded by cross-phase modulation (XPM) especially in materials with a high n_2 value like for AGSe [8, 21]. Thus, intensity-to-phase noise of the driving pulse could be transferred into the generated idler. The measured fluctuations of the driving pulses are ~2.5% rms and the estimated B-integral value of the idler beam, which is mainly influenced by pump-idler XPM, is less than ~15 rad. Mücke *et al.* [21] generated CEP-stable signal pulses in an OPA at B-integral value of ~10 rad and pump energy fluctuations of 1.2% (rms). Recently, the intrinsic CEP stability of an idler pulse at 4.5-9.0 μm in a passive CEP-stable mid-IR OPA has been confirmed using *f*-3*f* cross-referencing spectral interferometry [4]. Therefore, we believe the CEP in the current intrapulse DFG is maintained. In this work, however, the experimental characterization has not been attempted due to the marginally low pulse energy (2 μJ) for the *f*-3*f* spectral

interferometry. In addition, parasitic optical parametric generation having arbitrary phase could also adversely affect the CEP stability of the idler pulse [8].

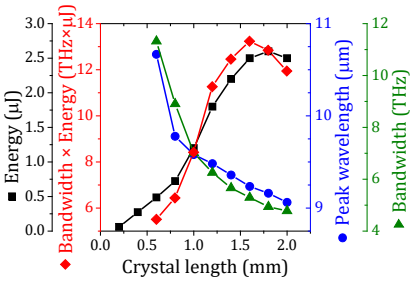

Fig. 4 (Color online) Calculated dependence of energy, peak wavelength, bandwidth (FWHM), and bandwidth-energy product on crystal length. Each color relates to the vertical axis of the same color.

Though a relatively high conversion efficiency has been achieved, a sub-optimal crystal length may limit the bandwidth and efficiency due to group velocity mismatch (GVM). We calculate the peak wavelength, bandwidth, and pulse energy in dependence on crystal length for 30 fs long drive pulses at a fixed laser intensity (Fig. 4). 71% of the total pulse energy is in the *e*-wave, which is found to be optimal for the 2-mm-thick crystal. The peak wavelength shifts to shorter wavelengths with increasing crystal length. This is attributed to the gradual broadening of driver's spectral bandwidth with the pulse propagation due to SPM along with the amplification of longer parts of the driver spectrum (signal part). The idler bandwidth decreases with the propagation due to GVM. The idler pulse energy increases with crystal length and starts rolling over at 1.8 mm. The highest product of the idler bandwidth and pulse energy, *i.e.*, measure of peak power, is obtained for 1.6 mm of length. Global optimization requires a comprehensive 3-dimensional search (laser intensity, input polarization, and crystal length).

In conclusion, we used few-cycle 2.1-μm pulses for driving intrapulse DFG in a type-II AGSe crystal. The idler pulses centered at 8.5 μm with a bandwidth of 1.4 μm (FWHM) were generated with 0.8% conversion efficiency. We believe this is the first time the ~2 μm beam was used for intrapulse DFG. The experimental results are consistent with numerical calculations of intrapulse DFG with blueshift, which was accompanied by spectral broadening of the drive pulse via SPM. Theses longer mid-IR pulses can be used for seeding of CEP-stable few-cycle OPCPA's as well as for strong-field experiments in nanostructures and solids.

Funding. European Regional Development Fund and the state budget of the Czech Republic (CZ.02.1.01/0.0/0.0/15_006/0000674); European Union's Horizon 2020 research and innovation programme (739573); Ministry of Education, Youth and Sports of the Czech Republic (LO1602, LM2015086); Czech Science Foundation (GA16-12960S); US AFOSR (FA9550-12-1-0499, FA9550-14-1-0255); US DOE accelerator stewardship program (DE-SC0018378); the CFEL, DESY, Hamburg, Germany, and the excellence cluster "The Hamburg Centre for Ultrafast Imaging—Structure, Dynamics and Control of Matter at the Atomic Scale" of the Deutsche Forschungsgemeinschaft.

Acknowledgment. We thank Dr. T. Lang for letting us use the 2 + 1 dimensional nonlinear pulse propagation analyzer [19].

References

1. T. Popmintchev, M.-C. Chen, D. Popmintchev, P. Arpin, S. Brown, S. Ališauskas, G. Andriukaitis, T. Balčiunas, O. D. Mücke, A. Pugzlys, A. Baltuška, B. Shim, S. E. Schrauth, A. Gaeta, C. Hernández-García, L. Plaja, A. Becker, A. Jaron-Becker, M. M. Murnane, and H. C. Kapteyn, Science **336**, 1287 (2012).
2. G. J. Stein, P. D. Keathley, P. Krogen, H. Liang, J. P. Siqueira, C.-L. Chang, C.-J. Lai, K.-H. Hong, G. M. Laurent, and F. X. Kärtner, J. Phys. B: At., Mol. Opt. Phys. **49**, 155601 (2016).
3. S. Ghimire, A. DiChiara, E. Sistrunk, P. Agostini, L. DiMauro, and D. Reis, Nat. Phys. **7**, 138 (2011).
4. H. Liang, P. Krogen, Z. Wang, H. Park, T. Kroh, K. Zawilski, P. Schunemann, J. Moses, L. F. DiMauro, F. X. Kärtner, and K.-H. Hong, Nat. Commun. **8**, 141 (2017).
5. T. Rybka, M. Ludwig, M. F. Schmalz, V. Knittel, D. Brida, and A. Leitenstorfer, Nat. Photonics **10**, 667 (2016).
6. W. Putnam, R. Hobbs, P. Keathley, K. Berggren, and F. X. Kärtner, Nat. Phys. **13**, 335 (2017).
7. A. Baltuška, T. Fuji, and T. Kobayashi, Phys. Rev. Lett. **88**, 133901 (2002).
8. G. Cerullo, A. Baltuška, O. Mücke, and C. Vozzi, Laser Photonics Rev. **5**, 323 (2011).
9. Y. Deng, A. Schwarz, H. Fattahi, M. Ueffing, X. Gu, M. Ossiander, T. Metzger, V. Pervak, H. Ishizuki, T. Taira, T. Kobayashi, G. Marcus, F. Krausz, R. Kienberger, and N. Karpowicz, Opt. Lett. **37**, 4973 (2012).
10. K.-H. Hong, C.-J. Lai, J. Siqueira, P. Krogen, J. Moses, C. Chang, G. Stein, L. Zapata, and F. Kärtner, Opt. Lett. **39**, 3145 (2014).
11. T. Zentgraf, R. Huber, N. Nielsen, D. Chemla, and R. Kaindl, Opt. Express **15**, 5775 (2007).
12. Y. Yin, X. Ren, A. Chew, J. Li, Y. Wang, F. Zhuang, Y. Wu, and Z. Chang, Sci. Rep. **7**, 11097 (2017).
13. I. Pupeza, D. Sanchez, J. Zhang, N. Lilienfein, M. Seidel, N. Karpowicz, T. Paasch-Colberg, I. Znakovskaya, M. Pescher, W. Schweinberger, V. Pervak, E. Fill, O. Pronin, Z. Wei, F. Krausz, A. Apolonski, and J. Biegert, Nat. Photonics **9**, 721 (2015).
14. G. Krauss, D. Fehrenbacher, D. Brida, C. Riek, A. Sell, R. Huber, and A. Leitenstorfer, Opt. Lett. **36**, 540 (2011).
15. D. Sanchez, M. Hemmer, M. Baudisch, S. L. Cousin, K. Zawilski, P. Schunemann, O. Chalus, C. Simon-Boisson, and J. Biegert, Optica **3**, 147 (2016)
16. T. Kanai, P. Malevich, S. S. Kangaparambil, K. Ishida, M. Mizui, K. Yamanouchi, H. Hoogland, R. Holzwarth, A. Pugzlys, and A. Baltuska, Opt. Lett. **42**, 683-686 (2017).
17. K. Murari, G. Cirmi, B. Debord, H. Cankaya, F. Gerome, A. Rühl, I. Hartl, F. Benabid, O. Mücke, and F. X. Kärtner, in Lasers Congress 2016 (ASSL, LSC, LAC) (Optical Society of America, 2016), p. AW1A.5.
18. S. B. Mirov, V. V. Fedorov, D. Martyshkin, I. S. Moskalev, M. Mirov, and S. Vasilyev, IEEE J. Sel. Top. Quantum Electron. **21**, 292 (2015).
19. T. Lang, A. Harth, J. Matyschok, T. Binhammer, M. Schultze, and U. Morgner, Opt. Express **21**, 949 (2013).
20. S. Marzenell, R. Beigang, and R. Wallenstein, Appl. Phys. B: Lasers Opt. **69**, 423 (1999).
21. O. Mücke, D. Sidorov, P. Dombi, A. Pugzlys, A. Baltuska, S. Alisauskas, V. Smilgevicius, J. Pocius, L. Giniunas, R. Danielius, and N. Forget, Opt. Lett. **34**, 118 (2009).